

View PDF Version Previous Article Next Article



DOI: <u>10.1039/C8TA00804C</u> (Paper) <u>J. Mater. Chem. A</u>, 2018, **6**, 7027-7033

# *In situ* lithiated quinone cathode for ALD/MLD-fabricated high-power thin-film battery<sup>†</sup>

Mikko Nisula and Maarit Karppinen 匝\*

Department of Chemistry and Materials Science, Aalto University, 00076 Aalto, Finland. E-mail: maarit.karppinen@aalto.fi

Received 25th January 2018 , Accepted 27th March 2018

First published on 29th March 2018

## Abstract

We demonstrate that the high-capacity organic electrode material, *p*-benzoquinone, is able to sustain ultrahigh redox reaction rates without any conductive additives when applied as ultrathin layers in an all-solid-state thin-film battery setup, viable for *e.g.* high-performance power sources in microelectronic devices. The combined atomic/molecular layer deposition (ALD/MLD) technique employed for the fabrication allows the *in situ* deposition of the quinone cathode in its lithiated state. The LiPON solid electrolyte is fabricated by ALD as a remarkably thin layer down to 30 nm. Our proof-of-concept setup is able to reach 50% of the full capacity in less than 0.25 s, with energy/power densities of 108 mW h cm<sup>-3</sup> and 508 W cm<sup>-3</sup>. These characteristics are of considerable promise towards bridging the gap between microbatteries and microsupercapacitors. Moreover, we demonstrate an all-ALD/MLD-made organic battery where the lithium quinone and LiPON layers are combined with a lithium terephthalate anode layer.

### **1. Introduction**

Organic Li-ion battery electrode materials such as quinones have gained interest due to their low-cost, abundant and environmentally benign constituents, and high specific capacity, but in bulk form their poor electronic conductivity significantly hinders the rate performance.<sup>1,2</sup> Enhanced redox kinetics have been achieved with surface functionalization of carbonaceous and conductive polymer substrates with quinone moieties for both battery<sup>3,4</sup> and supercapacitor applications,<sup>5–7</sup> but only at the cost of a significantly reduced energy density. Thin films can be seen as an intermediate between the conventional bulk and the surface-functionalized materials, and thus as a promising platform to fuse some of the benefits from the two extremes.

For an organic n-type cathode material, the quinone family provides the most prominent candidates. Quinones can undergo a twostep reduction by enolization of the carbonyl groups with a semiquinone radical intermediate product (Fig.\_1(a)). The dianion is stabilized by charge delocalization within the conjugated system, and the negative charge is balanced by ion-coordination to cations such as Li<sup>+</sup>. The simplest member of the quinone family is *p*-benzoquinone (BQ). With its theoretical maximum capacity of 496 mA h g<sup>-1</sup> and the relatively high redox potential of 2.8 V *vs.* Li/Li<sup>+</sup>, BQ also ranks high regarding the electrochemical performance. However, its high solubility in liquid electrolytes practically prevents its use in conventional wet-cell Li-ion batteries.<sup>8,9</sup> Obviously, in an all-solidstate thin film setup the dissolution issue is completely avoided.

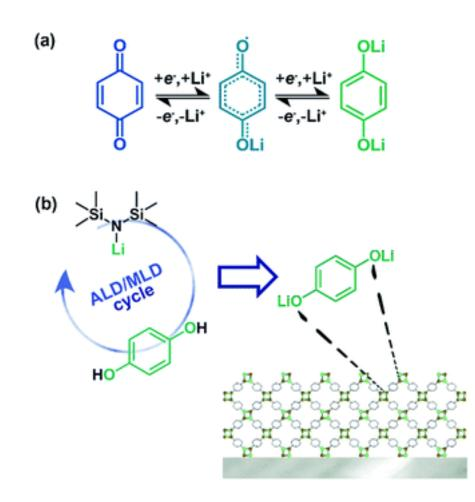


**Fig. 1** (a) The redox scheme of p-benzoquinone. (b) The ALD/MLD process for the Li<sub>2</sub>Q thin films.

Recently, we demonstrated that high-quality Li-organic thin films can be deposited using the combined atomic/molecular layer deposition (ALD/MLD) technique; our pioneering work moreover revealed excellent electrochemical performance for the lithium terephthalate anode material.<sup>10</sup> A major difficulty in using the quinones as cathode materials in a Li-ion battery is that they do not contain lithium in their neutral form. Here we demonstrate that the ALD/MLD approach is commendably suited for the *in situ* deposition of the lithiated, dianionic (*i.e.* discharged) form of BQ by deprotonating the hydroquinone (HQ) organic precursor molecules with lithium bis(trimethylsilyl)amide (LiHMDS) used as the source of lithium; in this process hexamethyldisilazane is released as the volatile by-product (Eig.\_1(b)). The surface saturation limited layer-by-layer process yields high-quality thin films of dilithium-1,4-benzenediolate (Li<sub>2</sub>Q) with nanometer-scale thickness control.<sup>11</sup>

Also importantly, the recent progress in ALD of solid electrolyte materials and in particular lithium phosphorous oxynitride (LiPON)<sup>12,13</sup> has enabled the manufacturing of all-solid-state thin-film batteries with sub-100 nm thick electrolyte layers;<sup>14,15</sup> this is the key requirement in high-power applications. Now, in the present work we demonstrate that combining the LiHMDS–HQ process for Li<sub>2</sub>Q with our previously reported ALD LiPON process,<sup>12</sup> we are able to manufacture all-solid-state thin-film batteries with an organic cathode material without relying on an external lithium source in the cell setup. For the negative electrode, the cells rely on the *in situ* formed metallic Li – a concept earlier introduced by Neudecker *et al.*<sup>16</sup> for an inorganic thin-film battery. Namely, during the first charge of the cell, a layer of Li forms on the Cu negative current collector, which is then consumed on the discharge. Despite the insulating nature of quinone molecules, the thin-film approach allows for the use of extremely high C-rates up to 6500. In addition, by using our previously reported ALD/MLD-fabricated lithium terephthalate as the negative electrode, we demonstrate an all-organic solid-state thin-film battery capable of extended charge–discharge cycling.

## 2. Experimental

The cell manufacturing was carried out in three phases. First, 300 mm Si wafers were coated with 500 ALD cycles (~23 nm) of Pt using (methylcyclopentadienyl)trimethylplatinum and oxygen as reported elsewhere.<sup>17</sup> The Pt depositions were carried out with a Picosun R-200 Advanced ALD-reactor. The wafers were then cut into  $3 \times 3 \text{ cm}^2$  pieces, and the Li<sub>2</sub>Q and LiPON layers were deposited on top of the Pt layer in succession without breaking the vacuum in between. These depositions were carried out in an F-120 flow-type hot-wall ALD reactor (ASM Microchemistry Ltd.) using our previously reported ALD/MLD processes.<sup>11,12</sup> In short, the Li<sub>2</sub>Q layers were deposited using LiHMDS (97%, Sigma-Aldrich) and hydroquinone (HQ, >99%, Sigma-Aldrich) as the precursors. The deposition temperature was 160 °C with pulse/purge times of 2 s/2 s and 10 s/20 s for LiHMDS and HQ, respectively. The LiPON layer was deposited at 300 °C using LiHMDS and diethyl phosphoramidate (DEPA) as the precursors with pulse/purge times of 2 s/2 s for both precursors. For sufficient volatility, LiHMDS, HQ and DEPA were heated to 60, 95 and 85 °C, respectively.

With each sample, two reference substrates (Si(100) and Pt) were simultaneously coated for the sake of characterization. The Si

reference substrate was required as in scanning electron microscopy (SEM) cross-section images the contrast between LiPON and  $Li_2Q$  was not sufficient to discern their individual layer thicknesses, while in the X-ray reflectivity (XRR) measurements the high density Pt substrate hindered the analysis of the other layers of the whole cell. A corner of each Pt substrate was masked with a piece of silicon wafer to preserve electric contact to the electrode. After the LiPON deposition, the samples were transferred to a Leybold-Heraeus Univex-300 thermal evaporator, which was used to deposit the Cu top contacts (~70 nm thickness, diameter = 3 mm) using a shadow mask resulting in 20–30 individual cells per sample. The  $Li_2Q/LiPON/Ge$  cell was manufactured similarly, with an addition of Cu current collector for the Ge electrode. Due to incompatible deposition processes, the  $Li_2Q-Li_2TP$  cells were manufactured with the following deposition order:  $Pt/Li_2TP/LiPON/Li_2Q/Cu$ . The  $Li_2TP$  layer (70 ALD/MLD cycles) was deposited at 200 °C using the previously reported process<sup>10</sup> with the exception that LiHMDS was used as the lithium precursor. During the transfer from the ALD reactor to the evaporator, all the samples were exposed to ambient air for several minutes.

The presence of  $Li_2Q$  and LiPON in the samples was confirmed using Fourier transform infrared spectroscopy (FTIR; Nicolet Magna 750, transmission mode, 400–4000 cm<sup>-1</sup>, 4 cm<sup>-1</sup> resolution), which also allowed semiquantitative analysis on the layer thickness. The layer thicknesses were obtained from X-ray reflectivity (XRR, PANanalytical X'Pert Pro, Cu K<sub> $\alpha$ </sub> X-ray source) measurements. The individual layer thicknesses were obtained by fitting the XRR data from the Si(100) substrate. The SEM images were acquired with a Tescan Mira3 FE-SEM.

The electrochemical measurements were carried out using an Autolab PGSTAT302N potentiostat/galvanostat. Given the limited cycle life of the *in situ* anode design, a pristine cell was used for each measurement (*i.e.* for each scan rate/current density). The contact to the top electrode was made using a self-made spring-loaded Pt wire.

#### 3. Results and discussion

The structure of our Li<sub>2</sub>Q/LiPON/Cu cells deposited on platinum is schematically shown in Fig. 2(a). The thickness of the Li<sub>2</sub>Q cathode layer was varied from 5 to 42 nm, while the thickness of the LiPON electrolyte layer was kept at 30 nm, unless otherwise mentioned. In our original work where the ALD/MLD process of Li<sub>2</sub>Q was developed the films of the same thickness scale as investigated here were crystalline;<sup>11</sup> nevertheless, all the present films deposited on Pt substrates were seemingly amorphous. From FTIR, the presence of both Li<sub>2</sub>Q and LiPON in the samples was confirmed, with the absorption intensities scaling linearly with the respective layer thickness as expected, see Fig. 2(b) and S1(b);† reference FTIR spectra of Li<sub>2</sub>Q and LiPON are shown in Fig. S1(a).† The individual layer thicknesses were determined from parallel samples grown on silicon by fitting the XRR patterns with a three-layer model consisting of the Si substrate, Li<sub>2</sub>Q, and LiPON layers. An exemplary fit of XRR data is shown in Fig. 2(c). The results yielded the expected linear behavior of thickness as a function of the number of ALD/MLD cycles (inset, Fig. 2(c)). The linear growth was also confirmed for LiPON (Fig. S2(a)†). The layer roughness, as judged from the XRR fit, is in the range of 1 to 2.5 nm in our films (Fig. S2(b)†).

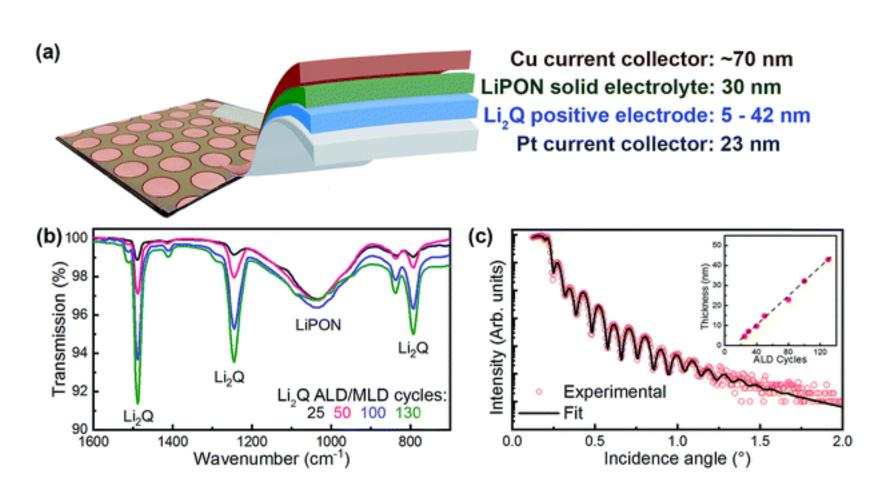


**Fig. 2** (a) Schematic presentation of the Li<sub>2</sub>Q/LiPON/Cu cells used to evaluate the electrochemical performance of Li<sub>2</sub>Q. The *in situ* Li negative electrode is electroplated on the Cu current collector upon the first charge of the cell. (b) FTIR spectra confirming the presence of both Li<sub>2</sub>Q and LiPON in the samples. (c) Representative XRR fit used to extract the individual layer thicknesses in a Li<sub>2</sub>Q/LiPON stack. The inset demonstrates the expected linear dependence of the Li<sub>2</sub>Q layer thickness on the number of deposition cycles.

Cyclic voltammetry (CV) and chronopotentiometry were used to establish the electrochemical activity of the Li<sub>2</sub>Q films. As the cell design prevented the use of a reference electrode the results reflect the properties of the whole cell instead of solely arising from the Li<sub>2</sub>Q positive electrode. Hence the results are treated in terms of the terminal voltage of the cell. In Fig. S3(a)<sup>†</sup> we present a voltammogram recorded for a 10 nm sample at 0.2 mV s<sup>-1</sup> from 0.1 to 4 V. A single prominent oxidation peak is seen at 3.38 V on the initial anodic sweep, whereas on the return sweep, the reduction occurs in two phases such that the more prominent is seen peak at 2.57 V with an overlapping shoulder at 2.49 V. With the theoretical maximum capacity of 439.5 mA h g<sup>-1</sup> and assuming a density of 1.2 g cm<sup>-3</sup> as determined from XRR measurements, the total integrated charge  $Q_{\text{Ox total}}$  obtained from the 10 nm layer should be 0.50  $\mu$ A h cm<sup>-2</sup>. The total charge for the anodic sweep is 1.0 μA h cm<sup>-2</sup>, and for the cathodic sweep 0.53 μA h cm<sup>-2</sup>. However, the area under the anodic peak  $Q_{\text{Ox,peak}}$  (onset determined from the first derivative of the curve) is 0.48  $\mu$ A h cm<sup>-2</sup>, while being only 0.35  $\mu$ A h cm<sup>-2</sup> for the cathodic peak. Parallel behavior is seen with the chronopotentiometric measurements. On the first charging of the cell at 2 µA cm<sup>-2</sup>, the obtained capacity 1.0  $\mu$ A h equals to the  $Q_{Ox,total}$  of the CV measurement, whereas the total discharge capacity is 0.55  $\mu$ A h cm<sup>2</sup>. The coulombic efficiency is improved on the subsequent cycles, where also the charge capacity is close to the theoretical maximum (Fig. S3(b)<sup>†</sup>). The charge plateau occurs at 3.29 V, whereas from the discharge curve two plateaus at 2.57 and 2.43 V are discerned in an agreement with the CV data. The linear change in the potential at the end of discharge is tentatively ascribed to double-layer capacitance. The capacity associated with the plateaus exactly matches those of the anodic/cathodic peak in the CV measurements. Therefore, we ascribe the initial excess charge capacity of ~0.46 µA h cm<sup>-2</sup> on a parasitic side reaction. In our additional tests with a Pt/LiPON/Cu setup, the initial charging capacity corresponds to the excess capacity observed in the Li<sub>2</sub>Q sample with little subsequent electrochemical activity (Fig. S3(c)<sup>†</sup>). In Fig. S3(d) and S4(e),<sup>†</sup> the irreversible oxidation is further confirmed with cyclic voltammetry. On the first anodic sweep, two small peaks are seen at 1.5 and 2.3 V, which are not present on the subsequent cycles. The parasitic reaction is suspected to be due to the decomposition of LiPON at the solid electrolyte/negative electrode interface. Recent experimental and theoretical studies indicate that at low electrode potentials and in contact with metallic lithium LiPON decomposes to Li<sub>3</sub>N, Li<sub>2</sub>O and Li<sub>3</sub>P.<sup>18–20</sup> Unfortunately, we were not able to directly observe the decomposition products but our observations for the electrochemical behavior of the cells are consistent with the aforementioned interpretation. The decomposition is expected to be selflimiting due the formation of an inert SEI layer. Indeed, the excess capacity occurs only on the first charge, after which the cell capacity is relatively constant for the next cycles. Thus, judging from the values of  $Q_{\text{Ox,peak}}$  and the voltage plateau in the constant current measurement, we conclude that during the oxidation both the Li<sup>+</sup> ions of each quinone molecule are involved. Whether the process is fully reversible, cannot be conclusively established using the present method as the *in situ* formed Li anode is known to instill capacity loss during cycling.<sup>16</sup> Also in this study, post-mortem analysis of the cells using SEM revealed that upon cycling, the *in situ* formed Li layer penetrates into the Cu current collectors leaving behind deposits presumably of LiOH or Li<sub>2</sub>O. In previous works the formation of such deposits has been attributed to reaction with  $O_2/H_2O$  traces present in the glove box atmosphere. We found that the amount of the deposits depends on the current rate and the number of charge/discharge cycles, which is in line with the electrochemical measurement data (Fig. S5(a)-(c)).

The full capacity is achieved only for the thinnest electrode layers. As shown in Fig. 3(a), at a scan rate ( $\nu$ ) of 2 mV s<sup>-1</sup> the capacity follows the theoretical line only up to 10 nm thick Li<sub>2</sub>Q layers. From 15 nm up to 42 nm, the integrated charge associated with the anodic peak ( $Q_{0x,peak}$ ) remains constant at 0.55  $\mu$ A h cm<sup>-2</sup>. The corresponding voltammograms are shown in ESI Fig. S5(a).<sup>†</sup> The peak shift is highly asymmetric for the anodic sweep with  $\Delta E_{peak}$  values of up to 1 V, whereas a comparatively minor shift is observed for the cathodic peak position (ESI Fig. S5(b).<sup>†</sup>). The restricted cell capacity is not affected by the electrolyte layer thickness; increasing the thickness up to 90 nm increases the ohmic loss as is seen in the symmetric increase in the peak separation and peak broadening typical for an increased cell resistance (ESI Fig. S6.<sup>†</sup>). The redox peak area however stays constant. The same effect is observed also in the constant current charge/discharge curves, where at a current density of 2  $\mu$ A cm<sup>-2</sup> the capacity increases linearly only up to the 10 nm layer thickness and plateauing at 15 nm (ESI Fig. S7.<sup>†</sup>). When the current density is increased to 20  $\mu$ A cm<sup>-2</sup>, the difference in cell polarization between the 15 nm and 30 nm samples becomes apparent (ESI Fig. S8.<sup>†</sup>). Similar saturation of capacity has previously been observed for other quinone and nitroxide radical containing thin films.<sup>21,22</sup>

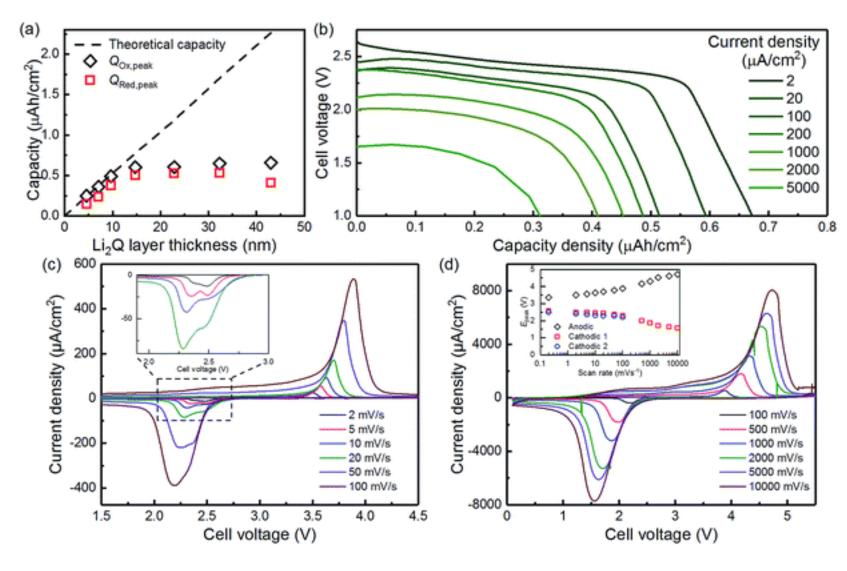


**Fig. 3** (a) Integrated capacity corresponding to the redox peaks of the solid-state cells as a function of  $Li_2Q$  layer thickness. The experimental values follow the theoretical maximum (dashed line) up to  $Li_2Q$  thickness of 10 nm. (b) Discharge voltage curves with current density ranging from 2  $\mu$ A cm<sup>-2</sup> (approximately 2.6C) to 5000  $\mu$ A cm<sup>-2</sup> (6500C) for  $Li_2Q$  layer thickness of 15 nm. (c and d) Cyclic voltammograms between 2 and 100 mV s<sup>-1</sup> and 100–10 000 mV s<sup>-1</sup>, respectively with  $Li_2Q$  layer thickness of 10 nm. The inset in (c) highlights the cathodic peak for the scan rates between 2 and 20 mV s<sup>-1</sup> whereas the inset in (d) shows the redox peak separation as a function of the scan rate.

Up to the  $Li_2Q$ -layer thickness of 15 nm the rate performance is excellent. The discharge voltage profiles measured at current rates from 2 to 5000 µA cm<sup>-2</sup> are shown in Fig. 3(b). Even at 5000 µA cm<sup>-2</sup> (C-rate of ~6500 assuming full theoretical capacity for a 15 nm thick  $Li_2Q$  layer), a discharge capacity of 0.31 µA h cm<sup>-2</sup> (or appr. 176 mA h g<sup>-1</sup>) is obtained. In other words, the cell is capable in delivering almost 50% of the initial capacity with a charge/discharge time of 0.25 s. The flat voltage profile is maintained even with the highest current rates. The rate capability exceeds even that of the ultrafast nitroxide radical thin films in aqueous media.<sup>23</sup> As the use of a solid electrolyte allows for high operation voltages in comparison to aqueous electrolytes and the voltage remains stable throughout the discharge, reasonably high energy density values can be obtained despite the ultrathin nature of the  $Li_2Q$  electrode. At 2 µA cm<sup>-2</sup>, an energy density of 1.55 µW h cm<sup>-2</sup> is obtained and even at 5000 µA cm<sup>-2</sup> one third of this, *i.e.* 0.51 µW h cm<sup>-2</sup>, is still obtained. The corresponding power densities range from 4.6 to 7265 µW cm<sup>-2</sup>. To widen the perspective, we should also look at the volumetric energy/power densities. At the low current density, the volumetric energy density reaches a value of 108 mW h cm<sup>-3</sup>, and at 5000 µA h cm<sup>-2</sup> the volumetric power density reaches 508 W cm<sup>-3</sup> while the energy density yet remains at the reasonably high value of 35.5 mW h cm<sup>-3</sup>. Here we should emphasize that the volumetric values were calculated using the volume of the full stack including the current collectors, even though the device is by no means optimized for the volumetric performance, *e.g.* the arbitrarily thick Cu current collector accounts in this setup for half of the total cell thickness.

To gain deeper comprehension of the seemingly fast charge storage, chronoamperometry and cyclic voltammetry measurements were conducted. In Fig. S9(a) and (b)<u>1</u> the chronoamperometric responses for charging and discharging are plotted as  $It^{0.5}vs$ . log t. The observed current transient is asymmetric regarding the oxidation and reduction with significantly faster reaction for the latter. With increasing Li<sub>2</sub>Q layer thickness, it seems that the redox reaction transition from kinetic to diffusion control. The integrated charge plotted against t shown in Fig. S9(c)<u>1</u> reveals that the reduction of the 10 nm films occurs very rapidly with 80% of the total capacity obtained in just 0.1 s. The CV measurements were conducted with scan rates from 0.2 to 10 000 mV s<sup>-1</sup>. As seen in Fig. 3(c) and (d), prominent redox peaks are visible all the way up to 10 000 mV s<sup>-1</sup>. The shift in the reduction peak potential is minimal up to 100 mV s<sup>-1</sup> (Fig. 3(c) and 2(d), insets). The  $Q_{0x,peak}$  remains constant at 0.5 µA h cm<sup>-2</sup> up to 2 V s<sup>-1</sup> implying fast redox reaction kinetics (Fig. S10<u>f</u>). To elucidate the nature of the charge storage, we plot (see ESI Fig. S11(a) and (b)<u>f</u>) the logarithm of the peak current density  $i_p$  against log(v): a slope value of 1 points towards capacitive charge storage according to

$$i = Cv$$
 (1

whereas a slope of 0.5 is expected for a purely diffusion controlled reaction as per the Randles–Sevcik equation

$$f_{\rm p} = 0.4463 n F c_{o,0} \sqrt{\frac{n F}{R T}} D^{0.5} v^{0.5}$$
(2)

Using the CV data from pristine cells, the slopes for the first/second cycle are determined to be 0.77/0.82 for the anodic current and 0.88/0.84 for the cathodic current 0.88/0.84. Above 2000 mV s<sup>-1</sup>, both the anodic and the cathodic current deviate from linearity. Based on the interpretation above, the current should be dominantly capacitive, yet the prominent redox peaks are clearly from a faradaic redox process. Fast faradaic redox reaction kinetics have been associated with pseudocapacitance,<sup>24</sup> but in the present case such a mechanism cannot be invoked as the redox peaks together with the voltage plateau in the galvanostatic measurements clearly indicate battery-like behavior.<sup>25,26</sup> Instead, a linear dependency of  $i_p$  versus v is also a fundamental property of molecular surface layers.<sup>27</sup> For surface films beyond a monolayer thickness, the surface-like dependency may persist depending on the efficiency of the charge carrier transport inside the film, and also the film thickness.<sup>28</sup> Considering the insulating nature of Li<sub>2</sub>Q, a possible explanation could be that the charge propagates through electron self-exchange of adjacent quinone molecules as has previously been observed for organic radical polymer layers.<sup>29</sup> Such a behavior would lead to a buildup of fully oxidized BQ molecules at the current collector/electrode interface, which at a certain thickness would terminate the efficient charge propagation, thus explaining the depressed performance observed for the cells with Li<sub>2</sub>Q layers thicker than 15 nm.

Another unexpected feature is the rather large voltage hysteresis, which is ill suited for high power applications. Previous experimental results indicate the redox potential of BQ to be ~2.8 V with no significant hysteresis between oxidation and reduction.<sup>8</sup> A rudimentary galvanostatic intermittent titration (GITT) measurement (ESI Fig. S12<u>1</u>) indicates that with the solid-state cells, the charge/discharge overpotential is indeed significant, *i.e.* 0.5/0.35 V, with the open circuit voltage close to the literature values. Here poor redox reaction kinetics are clearly ruled out as the underlying reason. Nucleation of metallic lithium could have some contribution but the overpotential for the nucleation is not likely to exceed some tens of millivolts.<sup>30</sup> A larger impact could arise from the phase transition within the Li<sub>2</sub>Q/BQ layer,<sup>31</sup> or alternatively as suggested by Precht *et al.*<sup>32</sup> from the electron transport across the metal–organic interface. Depending on the Fermi level alignment of the current collector with the HOMO and LUMO levels of the organic electrode, an electron injection barrier of several tenths of eV could form. As the HOMO–LUMO levels are dependent on the degree of lithiation,<sup>33</sup> the overpotential can be highly asymmetric regarding the charge/discharge. When Cu was utilized as the positive electrode current collector, only a very minor decrease in the cell polarization was observed (Fig. S13<u>1</u>). Further studies are needed to elucidate the origin of the unexpectedly large activation overpotential.

Finally, in Fig.4(a) we compare the capacity retention of our Li<sub>2</sub>Q solid-state device constructed with three different negative electrode schemes: the *in situ* plated Li, thermally evaporated Ge, and ALD/MLD-grown lithium terephthalate (Li<sub>2</sub>TP). With the *in situ* plated Li and Ge anodes, the cells lasted only for about 20 cycles before a rapid loss of capacity regardless of the current density used with an increase in the voltage polarization at each cycle (Fig. 4(b) and (c)). Electrochemical impedance spectroscopy (EIS) conducted at 5 charge/discharge cycle interval reveals that the cell impedance gradually increases upon cycling (Fig. S14(a),†). An additional component is seen in the Bode plots at end-of-life conditions (Fig. S14(b),†). However, given the two-electrode setup, its origin cannot conclusively be discerned. To complement the EIS measurements, post-mortem SEM analysis of the aged cells was also performed (Fig. S4(d-f),†). Significant amounts of deposits were observed on the anode current collector surface. In addition, the current collector itself was found to degrade, as cracking of the surface and erosion of the edges were clearly visible. Thus, the poor cycle life seems to stem from loss of lithium and degradation/delamination of the negative electrode current collector. In contrary, with Li<sub>2</sub>TP as the anode the cell performs more evenly retaining ~74% of the initial capacity over 100 charge/discharge cycles. The improved performance further suggest that the poor cycle life of the Li and Ge cells is due to the negative electrode. Here we should stress that the present cell designs were rather primitive. For instance, with proper protective layers, cycle life of above 1000 charge/discharge cycles has been achieved with an *in situ* plated Li anode with sputtered LiCoO<sub>2</sub> cathode and LiPON solid electrolyte.<sup>16</sup>

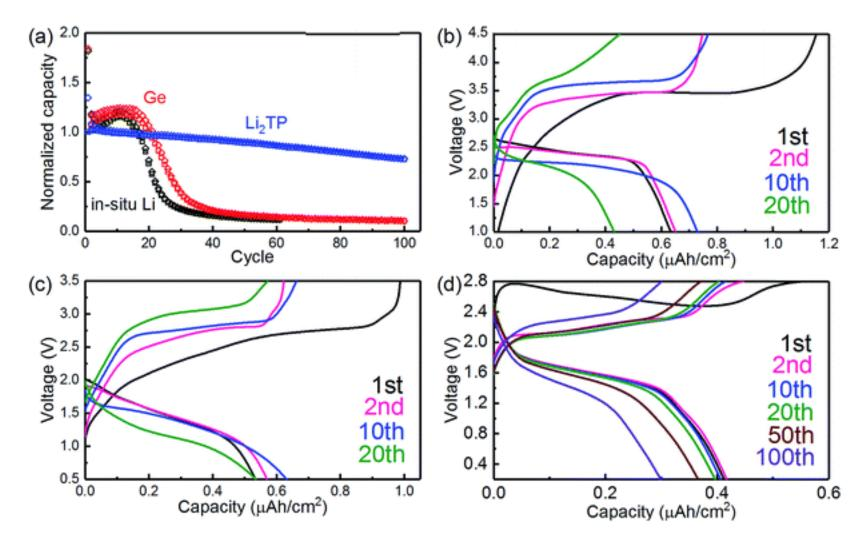


**Fig. 4** (a) Comparison of the cycling stability of the all-solid-state cells with different anode materials; *in situ* formed Li (black), germanium (red) and lithium terephthalate (blue). The open diamond/square markers represent the charge/discharge capacity, respectively. For visualization purposes, the data is normalized to the initial discharge capacity; 0.63, 0.54, and 0.41 μA h cm<sup>-2</sup> for *in situ* Li, Ge, and Li<sub>2</sub>TP, respectively. The corresponding voltage profiles are shown in (b) for *in situ* Li, (c) for Ge, and (d) for Li<sub>2</sub>TP.

## 4. Conclusions

We have presented ultrathin quinone thin films as an exciting cathode material for the all-solid-state thin-film Li-ion battery. Atomic/molecular layer deposition allows the fabrication of these films with a high precision and with the remarkable advantage that the cathode can be prepared in the lithiated form, thus simplifying the scheme, as the cells do not require any post-deposition lithiation treatments. Moreover, our organic all-solid-state cells are fully functional without any conductive additives; this fact could be of great benefit in fundamental studies on *e.g.* the redox kinetics. Most impressively, the work has demonstrated that nanoscaling is indeed the access to the extremely high redox reaction rate of quinones that further benefit from the ultra-thin solid electrolyte layer made possible by the ALD approach. Even though the cycle life of the current devices leaves much to improve on, we believe that the concept presented here could be an important step towards devices merging the energy density of batteries with the power density of supercapacitors.

## **Conflicts of interest**

The authors declare no competing financial interests.

#### Acknowledgements

The present work has received funding from the European Research Council under the European Union's Seventh Framework Programme (FP/2007-2013)/ERC Advanced Grant Agreement (No. 339478) and under the European Union's Horizon 2020 research and innovation Programme ERC Proof-of-Concept Grant Agreement (No. 780041), and also from the Academy of Finland through the Regular Research Project (No. 296299) and Strategic Research Council Project (No. 303452). We thank Picosun Oy for kindly providing the platinum-coated substrates. Ms Taina Rauhala is thanked for her assistance with the SEM experiments.

#### References

- 1. Y. Liang, Z. Tao and J. Chen, *Adv. Energy Mater.*, 2012, **2**, 742–769 CrossRef CAS **A**.
- 2. B. Häupler, A. Wild and U. S. Schubert, *Adv. Energy Mater.*, 2015, **5**, 1402034 CrossRef
- 3. A. Jaffe, A. Saldivar Valdes and H. I. Karunadasa, *Chem. Mater.*, 2015, **27**, 3568–3571 CrossRef CAS
- 4. S. W. Lee, N. Yabuuchi, B. M. Gallant, S. Chen, B.-S. Kim, P. T. Hammond and Y. Shao-Horn, *Nat. Nanotechnol.*, 2010, **5**, 531–537 CrossRef CAS PubMed .
- 5. D. M. Anjos, J. K. McDonough, E. Perre, G. M. Brown, S. H. Overbury, Y. Gogotsi and V. Presser, *Nano Energy*, 2013, **2**, 702–712 CrossRef CAS **a**.
- 6. C. Karlsson, H. Huang, M. Strømme, A. Gogoll and M. Sjödin, *J. Electroanal. Chem.*, 2014, **735**, 95–98 CrossRef CAS **A**.
- 7. S. K. Kim, J. Cho, J. S. Moore, H. S. Park and P. V. Braun, Adv. Funct. Mater., 2016, **26**, 903–910 CrossRef CAS 🔺.
- 8. H. Senoh, M. Yao, H. Sakaebe, K. Yasuda and Z. Siroma, *Electrochim. Acta*, 2011, **56**, 10145–10150 CrossRef CAS
- 9. T. Yokoji, Y. Kameyama, N. Maruyama and H. Matsubara, *J. Mater. Chem. A*, 2016, **4**, 5457–5466 CAS 🔺.
- 10. M. Nisula and M. Karppinen, *Nano Lett.*, 2016, **16**, 1276–1281 CrossRef CAS PubMed **A**.
- 11. M. Nisula, J. Linnera, A. J. Karttunen and M. Karppinen, *Chem.–Eur. J.*, 2017, **23**, 2988–2992 CrossRef CAS PubMed **\***.
- 12. M. Nisula, Y. Shindo, H. Koga and M. Karppinen, *Chem. Mater.*, 2015, **27**, 6987–6993 CrossRef CAS 🎴.
- 13. A. C. Kozen, A. J. Pearse, C.-F. Lin, M. Noked and G. W. Rubloff, *Chem. Mater.*, 2015, **27**, 5324–5331 CrossRef CAS **\***.
- 14. A. J. Pearse, T. E. Schmitt, E. J. Fuller, F. El-Gabaly, C. F. Lin, K. Gerasopoulos, A. C. Kozen, A. A. Talin, G. Rubloff and K. E. Gregorczyk, *Chem. Mater.*, 2017, **29**, 3740–3753 CrossRef CAS
- 15. B. Put, M. J. Mees, N. Hornsveld, A. Sepúlveda, P. M. Vereecken, W. M. M. Kessels and M. Creatore, *ECS Trans.*, 2017, 75, 61–69 CrossRef
- 16. B. J. Neudecker, N. J. Dudney and J. B. Bates, *J. Electrochem. Soc.*, 2000, **147**, 517 CrossRef CAS **A**.
- 17. T. Aaltonen, M. Ritala, T. Sajavaara, J. Keinonen and M. Leskelä, *Chem. Mater.*, 2003, **15**, 1924–1928 CrossRef CAS **4**.
- 18. Y. Zhu, X. He and Y. Mo, *ACS Appl. Mater. Interfaces*, 2015, **7**, 23685–23693 CAS 🏝.
- 19. A. Schwöbel, R. Hausbrand and W. Jaegermann, *Solid State Ionics*, 2015, **273**, 51–54 CrossRef
- 20. B. Put, P. M. Vereecken and A. Stesmans, *J. Mater. Chem. A*, 2018, **6**, 4848–4859 **CAS .**
- 21. C. R. DeBlaise, K. Hernández-Burgos, K. E. Silberstein, G. G. Rodríguez-Calero, R. P. Bisbey, H. D. Abruña and W. R. Dichtel, *ACS Nano*, 2015, **9**, 3178–3183 CrossRef PubMed .
- 22. T. Suga, H. Konishi and H. Nishide, *Chem. Commun.*, 2007, 1730–1732 RSC <sup>1</sup>.
- 23. K. Koshika, N. Sano, K. Oyaizu and H. Nishide, *Chem. Commun.*, 2009, 836–838 RSC 3.
- 24. V. Augustyn, J. Come, M. A. Lowe, J. W. Kim, P.-L. Taberna, S. H. Tolbert, H. D. Abruña, P. Simon and B. Dunn, *Nat. Mater.*, 2013, **12**, 518–522 CrossRef CAS PubMed .
- 25. P. Simon, Y. Gogotsi and B. Dunn, *Science*, 2014, **343**, 1210–1211 CrossRef CAS PubMed .
- 26. T. Brousse, D. Belanger and J. W. Long, *J. Electrochem. Soc.*, 2015, **162**, A5185–A5189 CrossRef CAS
- 27. A. J. Bard and L. R. Faulkner, *Electrochemical Methods: Fundamentals and Applications*, John Wiley & Sons, Inc., New York, 2nd edn, 2001 Search PubMed .
- 28. C. Costentin, T. R. Porter and J. M. Savéant, ACS Appl. Mater. Interfaces, 2017, 9, 8649–8658 🔼 🔺
- 29. K. Oyaizu, Y. Ando, H. Konishi and H. Nishide, *J. Am. Chem. Soc.*, 2008, **130**, 14459–14461 CrossRef CAS PubMed **a**.
- 30. F. Sagane, K. I. Ikeda, K. Okita, H. Sano, H. Sakaebe and Y. Iriyama, *J. Power Sources*, 2013, **233**, 34–42 CrossRef CAS <sup>4</sup>.
- 31. A. M. Bond, S. Fletcher, F. Marken, S. J. Shaw and P. G. Symons, *J. Chem. Soc., Faraday Trans.*, 1996, **92**, 3925–3933 RSC A.
- 32. R. Precht, R. Hausbrand and W. Jaegermann, *Phys. Chem. Chem. Phys.*, 2015, **17**, 6588–6596 RSC .
- 33. K. C. Kim, T. Liu, S. W. Lee and S. S. Jang, *J. Am. Chem. Soc.*, 2016, **138**, 2374–2382 CrossRef CAS PubMed <sup>▲</sup>.

#### Footnote

† Electronic supplementary information (ESI) available: Supplementary graphs for initial electrochemical response of the solid-state cells, additional CV, chronoamperometry and charge/discharge graphs on the effect of varying Li<sub>2</sub>Q and LiPON layer thickness, cell capacity and log–log plots as a function of the CV scan rate, and GITT measurement details and results. See DOI: <u>10.1039/c8ta00804c</u>

This journal is  $\ensuremath{\mathbb{C}}$  The Royal Society of Chemistry 2018